

Kepler Object of Interest Network

I. First results combining ground and space-based observations of Kepler systems with transit timing variations

C. von Essen^{1,2}, A. Ofir^{2,3}, S. Dreizler², E. Agol^{4,5,6,7}, J. Freudenthal², J. Hernández⁸, S. Wedemeyer^{9,10}, V. Parkash¹¹, H. J. Deeg^{12,13}, S. Hoyer^{12,13,14}, B. M. Morris⁴, A. C. Becker⁴, L. Sun¹⁵, S. H. Gu¹⁵, E. Herrero¹⁶, L. Tal-Or^{2,18}, K. Poppenhaeger¹⁹, M. Mallonn²⁰, S. Albrecht¹, S. Khalafinejad²¹, P. Boumis²², C. Delgado-Correal²³, D. C. Fabrycky²⁴, R. Janulis²⁵, S. Lalitha²⁶, A. Liakos²², Š. Mikolaitis²⁵, M. L. Moyano D'Angelo²⁷, E. Sokov^{28,29}, E. Pakštienė²⁵, A. Popov³⁰, V. Krushinsky³⁰, I. Ribas¹⁶, M. M. Rodríguez S.⁸, S. Rusov²⁸, I. Sokova²⁸, G. Tautvaišienė²⁵, X. Wang¹⁵

(Affiliations can be found after the references)

Received 18/12/2017; accepted

ABSTRACT

During its four years of photometric observations, the Kepler space telescope detected thousands of exoplanets and exoplanet candidates. One of Kepler's greatest heritages has been the confirmation and characterization of hundreds of multi-planet systems via Transit Timing Variations (TTVs). However, there are many interesting candidate systems displaying TTVs on such long time scales that the existing Kepler observations are of insufficient length to confirm and characterize them by means of this technique. To continue with Kepler's unique work we have organized the "Kepler Object of Interest Network" (KOINet), a multi-site network formed by several telescopes spread among America, Europe and Asia. The goals of KOINet are to complete the TTV curves of systems where Kepler did not cover the interaction timescales well, to dynamically prove that some candidates are true planets (or not), to dynamically measure the masses and bulk densities of some planets, to find evidence for non-transiting planets in some of the systems, to extend Kepler's baseline adding new data with the main purpose of improving current models of TTVs, and to build a platform that can observe almost anywhere on the Northern hemisphere, at almost any time. KOINet has been operational since March, 2014. Here we show some promising first results obtained from analyzing seven primary transits of KOI-0410.01, KOI-0525.01, KOI-0760.01, and KOI-0902.01 in addition to Kepler data, acquired during the first and second observing seasons of KOINet. While carefully choosing the targets we set demanding constraints about timing precision (at least 1 minute) and photometric precision (as good as 1 part per thousand) that were achieved by means of our observing strategies and data analysis techniques. For KOI-0410.01, new transit data revealed a turn-over of its TTVs. We carried out an in-depth study of the system, that is identified in the NASA's Data Validation Report as false positive. Among others, we investigated a gravitationally-bound hierarchical triple star system, and a planet-star system. While the simultaneous transit fitting of ground and space-based data allowed for a planet solution, we could not fully reject the three-star scenario. New data, already scheduled in the upcoming 2018 observing season, will set tighter constraints on the nature of the system.

Key words. stars: planetary systems – methods: observational

1. Introduction

Transit observations provide a wealth of information about alien worlds. Beside the detection and characterization of exoplanets (e.g. Seager 2010), once an exoplanet is detected by its transits the variations of the observed mid-transit times can be used to characterize the dynamical state of the system (Holman & Murray 2005; Agol et al. 2005). The timings of a transiting planet can sometimes be used to derive constraints on the planetary physical and orbital parameters in the case of multiple transiting planets (Holman et al. 2010), to set constraints on the masses of the perturbing bodies (Ofir et al. 2014), and to characterize the mass and orbit of a non-transiting planet, with masses potentially as low as an Earth mass (Agol et al. 2005; Nesvorný et al. 2013; Barros et al. 2013; Kipping et al. 2014; Jontof-Hutter et al. 2015). For faint stars, this is extremely challenging to achieve by means of other techniques.

In the past three decades, non-Keplerian motions of exoplanets have been regularly studied from the ground and space (Rasio et al. 1992; Malhotra et al. 1992; Peale 1993;

Wolszczan 1994; Laughlin & Chambers 2001; Rivera et al. 2010; Holman et al. 2010; Lissauer et al. 2011a; Becker et al. 2015; Gillon et al. 2016). Some examples of ground-based transit timing variation (TTV) studies are WASP-10b (Maciejewski et al. 2011), WASP-5b (Fukui et al. 2011), WASP-12b (Maciejewski et al. 2013), and WASP-43b (Jiang et al. 2016). Accompanying the observational growth, theoretical and numerical models were developed to reproduce the timing shifts and represent the most probable orbital configurations (e.g., Agol et al. 2005; Nesvorný & Morbidelli 2008; Lithwick et al. 2012; Deck et al. 2014). There is no doubt about the detection power of the TTV method: given the mass of the host star, analyzing photometric observations we can sometimes retrieve the orbital and physical properties of complete planetary systems (Carter et al. 2012). However, the method requires sufficiently long baseline, precise photometry and good phase coverage.

From ground-based studies, which have focused on TTVs of hot Jupiters, there have already been some discrepant results (see e.g. Qatar-1, von Essen et al. 2013; Mislis et al. 2015; Collins et al. 2017), especially when small-sized telescopes are involved and TTVs of low amplitude are being measured

Send offprint requests to: cessen@phys.au.dk

(von Essen et al. 2016). Also, many follow-up campaigns of hot Jupiters could not significantly observe TTVs from the ground (see e.g. Steffen & Agol 2005; Fukui et al. 2016; Petrucci et al. 2015; Raetz et al. 2015; Mallonn et al. 2015, for TrES-1, HAT-P-14b, WASP-28b, WASP-14b, and HAT-P-12b respectively). However, hot Jupiters tend to be isolated from companion planets (Steffen et al. 2012b) so it does not come as a surprise that these studies have not resulted in convincing signals. It was with the advent of space-based observatories that a new era in the TTV quest started. In March 2009, NASA launched the Kepler space telescope (Borucki et al. 2010; Koch et al. 2010). The main goal of the mission was to detect Earth-sized planets in the so-called habitable zone, orbiting around stars similar to our Sun. The wide field of view allowed simultaneous and continuous monitoring of many thousands of stars for about four years. Surprisingly, Kepler showed a bounty of planetary systems with a much more compact configuration than our Solar System (Lissauer et al. 2014). About 20% of the known planetary systems present either more than one planet or more than one star (Fabrycky et al. 2014). Particularly, most multiple systems are formed by at least two planets and about one third of these appear to be close to mean motion resonant orbits (see Lissauer et al. 2011b). Thus, the long-term and highly precise observations provided by Kepler have been the most successful data source used to confirm and characterize planetary systems via TTVs. Preceding a very long list, the first example of outstanding TTV discoveries is Kepler-9 (Holman et al. 2010). Since then, several other planetary systems were confirmed, detected or even characterized by means of TTV studies (see e.g. Hadden & Lithwick 2014; Nesvorný et al. 2014). Classic examples are Kepler-11 (Lissauer et al. 2011a), Kepler-18 (Cochran et al. 2011), Kepler-19 (Ballard et al. 2011), Kepler-23 and Kepler-24 (Ford et al. 2012a), Kepler-25 to Kepler-28 (Steffen et al. 2012a), Kepler-29 to Kepler-32 (Fabrycky et al. 2012), and Kepler-36 (Carter et al. 2012). The list goes up to Kepler-87 (Ofir et al. 2014) and continues with K2, Kepler’s second chance at collecting data that will allow us to investigate planetary systems by means of TTVs (see e.g. Becker et al. 2015; Nespral et al. 2016; Jontof-Hutter et al. 2016; Hadden & Lithwick 2017). Mazeh et al. (2013) analyzed the first twelve quarters of Kepler photometry and derived the transit timings of 1960 Kepler objects of interest (KOIs). An updated analysis of Kepler TTVs using the full long-cadence data set can be found under Holczer et al. (2016). The authors found that 130 KOIs presented significant TTVs, either because their mid-transit times had a large scatter, showed a periodic modulation, or presented a parabola-like trend. Although ~ 80 KOIs showed a clear sinusoidal variation, for other several systems the periodic signal was too long in comparison with the time span of Kepler data to cover one full TTV cycle. As a consequence, no proper dynamical characterization could be carried out.

To overcome this drawback and expand upon Kepler’s heritage, in the framework of a large collaboration we organized the Kepler Object of Interest Network¹ (KOINet). The main purpose of KOINet is the dynamical characterization of selected KOIs showing TTVs. To date, the network is comprised of numerous telescopes and is continuously evolving. KOINet’s first light took place in March, 2014. Here we show representative data obtained during our first and second observing seasons that will highlight the need for KOINet. Section 2 shows the basic working structure of KOINet and the scientific milestones, Section 3 describes the observing strategy and the data reduction process.

Section 4 makes special emphasis to the fitting strategy of both ground and space-based data. In Section 5 we show KOINet’s achieved milestones, and we finish with Section 6, where we present our conclusions and a brief description of the future observing seasons of KOINet.

2. Kepler Object of Interest Network

2.1. Rationale

KOINet’s unique characteristic is the use of already existing telescopes, coordinated to work together towards a common goal. The data collected by the network will provide three major contributions to the understanding of the exoplanet population. First, deriving planetary masses from transit timing observations for more planets will populate the mass-radius diagram. The distribution of planetary radii at a given planetary mass is surprisingly wide, revealing a large spread in internal compositions (see e.g. Mordasini et al. 2012). New mass and radius determinations will provide new constraints for planet structure models. Furthermore, longer transit monitoring will set tighter constraints for the existence of non-transiting planets (Barros et al. 2014), providing a broader and deeper view of the architecture of planetary systems. Finally, a larger sample of well-constrained physical parameters of planets and planetary systems will provide better constraints for their formation and evolution (Lissauer et al. 2011b; Fang & Margot 2012).

KOINet is initially focusing its instrumental resources on 60 KOIs that require additional data to complete a proper characterization or validation by means of the TTV technique. Basic information on the selected KOIs can be seen in the left part of Table 2. The KOI target list was built up based on the work of Ford et al. (2012b), Mazeh et al. (2013), Xie (2013, 2014), Nesvorný et al. (2013), Ofir et al. (2014), and Holczer et al. (2016). The 60 KOIs were drawn from four groups, depending on the scientific insights that further observations were expected to provide.

For a pair of planets, an anti-correlation in the TTV signal is expected to occur. This is the product of conservation of energy and angular momentum and is stronger when the planetary pair is near mean-motion resonance (see e.g. Holman et al. 2010; Carter et al. 2012; Lithwick et al. 2012). The systems that present polynomial-shaped TTVs and show anti-correlated TTV signals are given the highest priority, independent of their status as valid planet candidates. In these cases, any additional data points in their parabolic-shaped TTVs can reveal a turnover point, allowing a more accurate determination of planetary masses. Further data will allow the analysis of the system’s dynamical characteristics. The systems that present anti-correlation and a sinusoidal variation, but are poorly sampled, have second priority (such as KOI-0880.01/02, a detailed analysis of the system is in prep). In this case, more data points will allow us to improve the dynamical analysis of these systems. Under third priority fall the KOIs with very long TTV periodicity. Additional data might shed some light into the constitution of these systems (for example, KOI-0525.01, Section 5.3). Finally, the lowest priority is given to those systems that have been already characterized, and the systems showing only one TTV signal (e.g., KOI-0410.01, Section 5.5). In the latter, under specific conditions the perturber’s mass and orbital period can be constrained, confirming its planetary nature or ruling it out (e.g., Nesvorný et al. 2013, 2014).

¹ koinet.astro.physik.uni-goettingen.de

2.2. Observing time

During the first two observing seasons (April-September, 2014 and 2015) an approximate total of 600 hours were collected for our project, divided between 16 telescopes and 139 observing events. Rather than following up all of the KOIs, we focused on the most interesting ones from a dynamical point of view. Although here we present a general overview of the data collected by KOINet and its performance, we will focus in the analysis of individual KOIs in upcoming publications.

2.3. Basic characteristics of KOINet's telescopes

Kepler planets and planet candidates showing TTVs generally present two major disadvantages for ground-based follow-up observations. On one hand, their host stars are relatively faint ($K_p \sim 12-16$). On the other hand, most of the KOIs reported to have large amplitude TTVs produce shallow primary transits. To collect photometric data with the necessary precision to detect shallow transits in an overall good cadence, most of KOINet's telescopes have relatively large collecting areas. This allows to collect data at a frequency of some seconds to a few minutes. Another observational challenge comes with the transit duration. For some of the KOIs the transit duration is longer than the astronomical night, especially bearing in mind that the Kepler field is best observable around the summer season, when the nights are intrinsically shorter. In these cases full transit coverage can only be obtained combining telescopes well separated in longitude. The telescopes included in this collaboration are spread between America, Europe and Asia, allowing almost 24 hours of continuous coverage. A world map including the telescopes that collected data during 2014 and 2015 can be found in Figure 1 and Table 1.

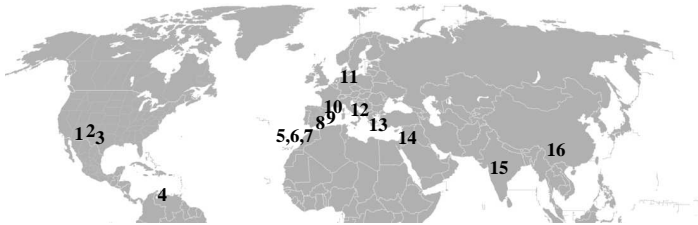


Fig. 1: World's northern hemisphere, showing approximate locations of the observing sites that acquired data for KOINet during the 2014 and 2015 seasons. Numbers correspond to Table 1.

Table 1: Placement of the observatories that collected data during the 2014 and 2015 observing seasons.

1	Multiple Mirror Telescope Observatory (6.5m), United States of America
2	Apache Point Observatory (3.5m), United States of America
3	Monitoring Network of Telescopes (1.2m), United States of America
4	Observatorio Astronómico Nacional del Llano del Hato (1m), Venezuela
5	Nordic Optical Telescope (2.5m), Spain
6	Liverpool Telescope (2m), Spain
7	IAC80 telescope (0.8m), Instituto de Astrofísica de Canarias, Spain
8	Calar Alto Observatory (1.25, 2.2, 3.5 m), Spain
9	Planetary Transit Study Telescope (0.6m), Spain
10	Joan Oró Telescope - The Montsec Astronomical Observatory (0.8m), Spain
11	Oskar Lühning Telescope - Hamburger Sternwarte (1.2m), Germany
12	Bologna Astronomical Observatory (1.52m), Italy
13	Kryoneri Observatory - National Observatory of Athens (1.2m), Greece
14	Wise Observatory - Tel-Aviv University (1m), Israel
15	IUCAA Girawali Observatory (2m), India
16	Yunnan Observatories (2.4m), China

Considering these two fundamental limitations, to maximize the use of KOINet data and boost transit detection we have included the KOIs whose transit depth are larger than one part per thousand (ppt) and which Kepler timing variability (this is, the variability comprised within Kepler time span) is larger than two minutes (see Figure 2). Below these limits, the photometric precision (and thus, the derived timing precision), and especially the impact of correlated noise on photometric data (Carter & Winn 2009) would play a fundamental role in the detection of transit events. Next, we describe the primary characteristics of the telescopes involved in this work.

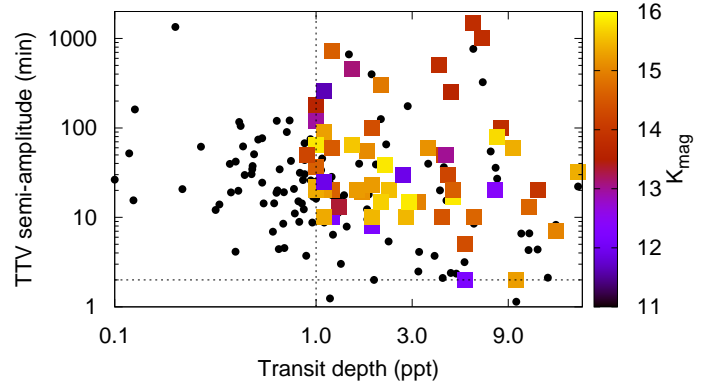


Fig. 2: Colored rectangles show TTV Kepler variability in minutes versus transit depth in ppt for the 60 KOIs that are included in KOINet. The squares are color-coded depending on the Kepler magnitude of the host star. Black circles show all the KOIs presenting TTVs with a Kepler variability larger than 1 minute. Vertical and horizontal dashed lines indicate the ~ 1 ppt and 2 minutes limits for KOINet.

- The Apache Point Observatory, located in New Mexico, United States of America, hosts the Astrophysical Research Consortium 3.5 meter telescope, henceforth ARC 3.5m. The data were collected using Agile (Mukadam et al. 2011). Concerning the data presented in this work, the ARC 3.5m observed one transit of KOI-0525.01, our lower-limit KOI for transit depth. Nonetheless, during the first observing seasons we have collected a substantial amount of data that will be presented in future work.
- The Nordic Optical Telescope (henceforth NOT 2.5m) is located at the observatory “Roque de los Muchachos” in La Palma, Spain, and belongs to the Nordic Optical Telescope Scientific Association, governed and funded by Scandinavian countries. In this work we present observations of KOI-0760.01 and KOI-0410.01.
- The 2.2m Calar Alto telescope is located in Almería, Spain (henceforth CAHA 2.2m). We observed KOI-0410.01 using the Calar Alto Faint Object Spectrograph in its photometric mode.
- The IAC80 telescope (henceforth, IAC 0.8m) is located at the Observatorio del Teide, in the Canary Islands, Spain. We observed half a transit of KOI-0902.01 for about 7 hours.
- The Lijiang 2.4m telescope (henceforth YO 2.4m) is located at the Yunnan Observatories in Kunming, China. In this work we present observations of KOI-0410.01.

2.4. Maximizing the use of KOINet's time

2.4.1. Assigning telescopes to KOIs

In order to effectively distribute the available telescope time and maximize our chances to detect transit events, three main characteristics have to be considered: the apparent magnitude of the host star, the available collecting area given by the size of the primary mirror, and the amplitude and scatter of Kepler TTVs. With the main goal to connect the KOIs to the most suitable telescopes, we proceed as follows. First, we estimate the exposure time, E_t , for each host star and telescope. The latter is computed to achieve a given signal-to-noise ratio (SNR), so that $\text{SNR} = 1/T_{\text{depth}}$ is satisfied. In this case, T_{depth} corresponds to the transit depth in percentage, which is taken from the NASA Exoplanet Archive². Besides the desired signal-to-noise ratio, the calculation of E_t is carried out considering parameters such as the mean seeing of the site, the brightness of the star, the size of the primary mirror, typical sky brightness of the observatories, the phase of the Moon, and the altitude of the star during the predicted observing windows. Once the exposure times are computed, the derived values are verified and subsequently confirmed by each telescope leader.

Off-transit data have a considerable impact in the determination of the orbital and physical parameters of any transiting system. In the case of ground-based observations, off-transit data are critical to remove systematic effects related to changes in airmass, color-dependent extinction, and poor guiding and flat-fielding (see e.g., Southworth et al. 2009; von Essen et al. 2016). Henceforth, to determine the number of data points per transit, N , we use the estimated exposure time and the known transit duration, T_{dur} , incremented by two hours. This increment accounts for 1 hour of off-transit data before and after transit begins and ends, respectively. Then, the number of data points per transit is simply estimated as $N = (T_{\text{dur}} + 2 \text{ hs}) / (E_t + \text{ROT})$. Here, ROT corresponds to the readout time of charge-coupled devices used to carry out the observations. To compute the timing precision, σ_T , we use a variant of the formalism provided by Ford & Holman (2007):

$$\sigma_T = \frac{\text{Phot}_p \times T_{\text{dur}}}{N^{1/2} \times T_{\text{depth}}}, \quad (1)$$

where Phot_p is the photometric precision in percentage that a given telescope can achieve while observing a 14–15 K_p star. This value was requested to the members of KOINet immediately after they joined the network. Comparing the estimated timing precision with the semi-amplitude of Kepler TTVs ($A_{\text{TTVs}} > 3\sigma_T$) yields erroneous results, especially if the TTVs are intrinsically large. For example, an estimated timing precision of one hour satisfies the above condition for a TTV semi-amplitude of 3 hours. However, when ground-based photometry is being analyzed, a timing precision of one hour would be equal to a non-detection. Therefore, to assign a KOI to a telescope three aspects are simultaneously considered: the transit depth ($T_{\text{depth}} > \text{Phot}_p$), the amplitude of Kepler TTVs ($A_{\text{TTVs}} > 3\sigma_T$), and the natural scatter of Kepler TTVs ($2\sigma_{\text{TTVs}} > \sigma_T$).

2.4.2. Prescription for optimum reference stars

Differential photometry highlights the variability of one star (the so-called target star) relative to another one (the reference star) which ideally should not vary in time. Thus, the selection

of reference stars can limit the precision of photometric data (Young et al. 1991; Howell 2006). The true constancy of reference stars is given by how much they intrinsically vary, subject to the precision that a given optical setup can achieve. Analyzing the flux measurements along the 17 quarters of all the stars within a radius of 5 arcmin relative to KOINet's KOIs, we selected stars that showed a constant flux behavior in time and had a comparable brightness to the given KOI (Howell 2006). In this way, we provide to the observer the location of the most photometrically well-behaved reference stars, minimizing the noise budget right from the beginning. Particularly, we have identified between 2 to 5 reference stars per field of view, and their location on sky are provided to the observers through KOINet's web interface.

2.5. Predictions computed from Kepler timings

Using the mid-transit times obtained from Kepler 17 quarters, we computed TTVs subtracting from them an averaged (constant) period, and classified the KOIs depending on the shape of their TTVs. A full description of the fitting process of Kepler transit light curves, the derived values, and their associated errors, can be found in Section 4.1. For now, Figure 3 shows our four target groups. The simplest case, in which the TTVs follow a sinusoidal shape, is shown on the top left panel of the Figure. To estimate the predictions for our ground-based follow-up we fitted to Kepler mid-transit times a linear plus a sinusoidal term:

$$\text{TTV}(E) = T_0(E = 0) + P_C \times E + A \times \sin[2\pi(\nu E + \phi)]. \quad (2)$$

In this case, E corresponds to the transit epoch, $T_0(E = 0)$ to a reference mid-transit time, P_C is the orbital (constant) period, A the semi-amplitude of the TTVs, and ν and ϕ the frequency and phase of the TTVs, respectively. The derived predictions are shown in Figure 3 in green points, while Kepler data is plotted in red and the shape of the predictions, including Kepler time, is shown in continuous black line. Since all Kepler mid-times show some scatter, we also estimated errors in the predictions taking this noise into consideration. To increase the chance of transit detection, the magnitudes of the errors in the predictions are provided to the observers, along with a warning. The second TTV scenario is shown in the top right panel of Figure 3. In this case the available data and the systems themselves allow a more refined dynamical analysis of the TTVs by means of n-body simulations and/or simultaneous transit fitting (see e.g., Agol et al. 2005; Nesvorný et al. 2013, 2014), from which the predictions are computed. Due to their complexity, a detailed description of the computation of these TTVs is beyond the scope of this paper, and will be given individually in future publications. The third case is shown in the bottom left panel of Figure 3. Here, the number of available Kepler transits is not sufficient to carry out a dynamical analysis, and the TTVs don't follow any shape that could give us a hint of when could the upcoming transits occur. Thus, to determine the predictions we fit to Kepler mid-times a linear trend only (i.e., assuming constant period), and use as errors for the predictions the semi-amplitude of the TTVs. The last case exemplifies the need for a ground-based campaign taking place immediately after Keplers follow-up. This case, displayed in the bottom right panel of Figure 3, shows an incomplete coverage of the TTV periodicity. From photometry only we cannot assess if the cause for TTVs is planetary in nature, is gravitationally bound to the system (e.g., TTVs following a sinusoidal shape), or some completely different scenario, like TTVs caused by a blended eclipsing binary (TTVs showing a parabolic shape).

² <https://exoplanetarchive.ipac.caltech.edu>

In this case, we produce two kind of predictions: sine TTVs, from where the predictions are computed as described in Eq. 2, and parabolic TTVs:

$$TTV(E) = T_0(E = 0) + P_C \times E + a \times E^2 + b \times E + c. \quad (3)$$

where a , b , and c are the fitting coefficients of the parabola. Although these are the two scenarios most likely to occur, the mid-times could also show a different trend. Therefore, until we can disentangle which trend is the one that the system follows, we provide to the observers both predictions and ask them to observe both of them, and extend the observing time as much as they can.

3. Observations and data reduction

3.1. Basic observing setup

In order to ensure observations as homogeneous as possible, observers are asked to carry them out in a specific way. To begin with, our observations cover a range of airmass and so are subject to differential extinction effects between the target and comparison stars. To minimize color-dependent systematic effects observers used intermediate (Cousins R) or narrow-band (gunn r) filters, depending on the brightness of the target stars and filter availability. The use of R-band filters also reduces light curve variations from starspots and limb-darkening effects, and they circumvent the large telluric contamination around the I-band. Furthermore, all observers provide regular calibrations (bias flatfield frames and darks, if needed), and are asked to observe with the telescope slightly defocused to minimize the noise in the photometry (Kjeldsen & Frandsen 1992; Southworth et al. 2009). Once the observations are performed, they are collected and reduced in an homogeneous way.

3.2. DIP²OL

KOINet data are reduced and analyzed by means of the *Differential Photometry Pipelines for Optimum Lightcurves*, DIP²OL. The pipeline is divided in two parts. The first one is based in IRAF's command language. It requires only one reference frame to do aperture photometry. The pipeline carries out normal calibration sequences (bias and dark subtraction and flat-field division, depending on availability) using IRAF task ccdproc. In the particular case of KOINet data, acquired calibrations are always a set of bias and flatfields, taken either at the beginning or end of each observing night. Subject to availability, we correct the science frames of a given observing night with their corresponding calibrations only. In general, we do not take dark frames due to short exposures and cooled, temperature stable CCDs. The reduction continues with cosmic rays rejection (IRAF's cosmicrays) and alignment of the science frames (imalign). Afterwards, reference stars within the field are chosen following specific criteria (for example, that the brightness of the reference stars have to be similar to the brightness of the target star to maximize the signal-to-noise ratio of the differential light curves, Howell 2006) and photometric fluxes and errors are measured over the target star and the reference stars as a function of 10 different aperture radii and 3 different sky rings. The annulus and the initial width of the sky ring are set by the user, since they depend on the crowding of the fields. The apertures are non-uniformly distributed between 0.5 and $5 \times \hat{S}$, with more density between 1 and $2 \times \hat{S}$. Here, \hat{S} corresponds to the averaged seeing of the images, computed from the full-width at half maximum of all the chosen stars in the field. This, in turn, sets a limit to

the lowest possible value for the annulus. To perform a posterior detrending of the photometric data, in addition to \hat{S} , the pipeline computes the airmass corresponding to the center of the field of view, the (x,y) centroid positions of all the measured stars, three sky values originally used to compute the integrated fluxes (one per sky ring), and the integrated counts of the master flat and master dark over the (x,y) values per frame and per aperture.

The second part of DIP²OL is python-based. The routine starts by producing N+1 light curves from the N reference fluxes previously computed by IRAF, one with the summed flux of all the N comparison stars and N versions with all the reference stars except one. If one of the reference stars is photometrically unstable, the residual light curve corresponding to the unweighted sum of the fluxes of all the reference stars minus this one will show up by giving the lowest standard deviation, when compared to the remaining N residuals. Therefore, this star is removed from the sample. The process of selection and rejection is repeated until the combination of the current available reference stars gives the lowest scatter in the photometry. Since a priori we don't know if primary transits are actually observed within a given predicted window, residuals are computed by dividing the differential fluxes by a spline function. The pipeline repeats this process through all measured apertures and sky rings, and finds the combination of reference stars, aperture and sky ring that minimizes the standard deviation of the differential light curves (see e.g., Ofir et al. 2014). Finally, the code outputs the time in Julian dates shifted to the center of the exposure, the differential fluxes, photometric error bars which magnitudes have been scaled to match the standard deviation of the residuals, (x,y) centroid positions, flat counts that were integrated within the final aperture around the given centroids, sky fluxes corresponding to the chosen sky ring, and seeing and airmass values. These quantities will be used in a following step to compute the ground-based detected mid-transit times.

4. Data modelling and fitting strategies

4.1. Primary transit fitting of Kepler data

One of the key ingredients for the success of our ground-based TTV follow-up is the prior knowledge, with a good degree of accuracy, of the orbital and physical parameters of the systems. To take full advantage of Kepler data in our work, we re-computed the orbital and physical parameters of the 60 KOIs that are included in KOINet's follow-up. A quick view into the Data Validation Reports suggested us that the procedures performed over KOIs without TTVs was not optimum for KOIs showing TTVs. Thus, we did not use the transit parameters reported by the NASA Exoplanet Archive. Rather than computing time-expensive photo-dynamical solutions over the 60 KOIs (see e.g., Barros et al. 2015), to minimize the impact of the TTVs in the computation of the transit parameters we fitted two consequent transit light curves simultaneously with a Mandel & Agol (2002) transit model, making use of their `occulquad` routine³. From the transit light curve we can determine the following parameters: the orbital period, P_{tr} , the mid-transit time, T_0 , the planet-to-star radius ratio, R_p/R_s , the semi-major axis in stellar radius, a/R_s , and the orbital inclination, i , in degrees. For all the KOIs we assumed circular orbits. Furthermore, we assumed a quadratic limb-darkening law with fixed limb darkening coefficients, u_1 and u_2 . For the Kepler data we used the limb-darkening values specified in Claret et al. (2013), choosing as fundamental stellar parameters, effective temperature,

³ <http://www.astro.washington.edu/users/agol>

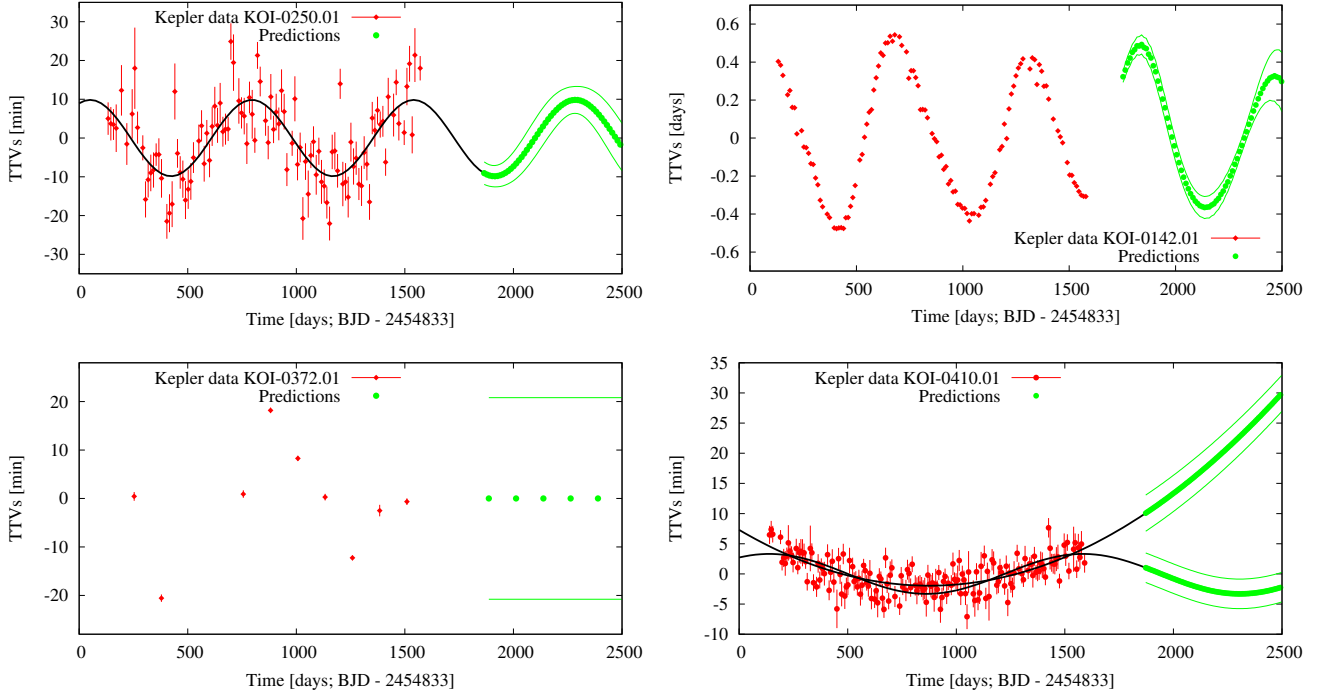


Fig. 3: *From left to right and top to bottom*: sinusoidal, dynamic, chaotic, and parabolic/sinusoidal classification of the TTVs. Note that TTVs for KOI-0142.01 are given in days, rather than minutes.

metallicity and surface gravity, the values listed in the NASA Exoplanet Archive. Simultaneously to the transit model we fitted a time-dependent second-order polynomial to account for out-of-transit variability. To determine reliable errors for the fitted parameters, we explored the parameter space by sampling from the posterior-probability distribution using a Markov-chain Monte-Carlo (MCMC) approach. Our MCMC calculations make extensive use of routines of `PyAstronomy`⁴, a collection of Python build-in functions that provide an interface for fitting and sampling algorithms implemented in the `PyMC` (Patil et al. 2010) and `SciPy` (Jones et al. 2001) packages. We refer the reader to their detailed online documentation⁵. For the computation of the best-fit parameters we iterated 80 000 times per consecutive transits, and discarded a conservative first 20%. As starting values for the parameters we used the ones specified in the NASA Exoplanet Archive. To set reasonable limits for MCMC’s uniform probability distributions, we chose $R_p/R_s \pm 0.1$, $T_0 \pm T_{\text{Dur}}/3$, and a considerable fraction of the orbital period, depending on the amplitude of Kepler TTVs. These values are relative to the values determined by the Kepler team. The semi-major axis and the inclination are correlated through the impact parameter, $a/R_s \cos(i)$. Thus, rather than using uniform distributions for these parameters we used Gaussian priors with the mean and the standard deviation equal to the values found in the NASA Exoplanet Archive and three times their errors, respectively. To compute the transit parameters we analyzed Kepler long cadence transit data. To minimize the impact of the sampling rate on the determination of the transit parameters (see e.g., Kipping 2010), during each instance of primary transit fitting we used a transit model calculated from a finer time scale and then averaged on the Kepler timing points. In partic-

ular, 30 equally spaced points were calculated and averaged to one data point. The modeling of all consecutive transits results in a parameter distribution for the semi-major axis, the inclination, the orbital period and the planet-to-star radius ratio. We used their mean values and standard deviations to limit the ground-based data fitting (Section 4.2). All the orbital and physical parameters computed for the 60 KOIs are summarized in the right part of Table 2. Errors are at the $1-\sigma$ level. It is worth to mention that the transit parameters presented in the table provide us with an excellent transit template to be used to fit ground-based data. It is not our intention to improve any of the parameters by means of this simple analysis. A more detailed approach, such as photodynamical fitting might be required (see e.g. Barros et al. 2015), specially with large-amplitude TTVs such as Kepler-9 (KOI-0377.01/02, Holman et al. 2010; Ofir et al. 2014). As an illustrative example, Figure 4 shows how the transit parameters change as a function of time, evidencing their mutual correlations and the rate and amplitude at which they change. As expected, for the values in the figure the Pearson’s correlation coefficient between the semi-major axis and the inclination is $r_{a/R_s, i} = 0.96$, while these two reveal a strong anti-correlation with the planet-to-star radius ratio ($r_{R_p/R_s, i} = -0.91$, and $r_{R_p/R_s, a/R_s} = -0.93$).

4.2. Primary transit fitting and detrending of ground-based data

Once `DIP2OL` returns the photometric light curve and the associated detrending quantities, the computation of ground-based TTVs begins. First, we convert the time-axis, originally given in Julian dates, to Barycentric Julian dates using Eastman et al. (2010) web tool¹. To do so, we make use of the celestial coordinates of the star, the geographic coordinates of the site, and the height above sea level. Throughout this work, our model com-

⁴ <http://www.hs.uni-hamburg.de/DE/Ins/Per/Czesla/PyA/PyA/index.html>

⁵ <http://pymc-devs.github.io/pymc/>

¹ <http://astroutils.astronomy.ohio-state.edu/time/utc2bjd.html>

Table 2: *Left:* From left to right the KOI number, the right ascension, α , and the declination, δ , in degrees (J2000.0) and the Kepler magnitude, K_p . The values have been taken from the NASA Exoplanet Archive. *Right:* Best-fit orbital parameters obtained fitting all available primary transits from quarter 1 to quarter 17 as described in this section. From left to right the semi-major axis in stellar radii, a/R_S , the inclination in degrees, i , the planet-to-star radius ratio, R_p/R_S , and the orbital period in days, Per. The last column, O14-15, corresponds to the number of observations collected during 2014 and 2015.

KOI Nr.	α (J2000) (°)	δ (J2000) (°)	K_p	a/R_S	i (°)	R_p/R_S	Per (days)	O14-15
0094.01	297.333069	41.891121	12.205	27.27 ± 0.03	89.997 ± 0.001	0.0691 ± 0.0001	22.34285 ± 0.00078	-
0094.03	297.333069	41.891121	12.205	50.5 ± 0.2	89.93 ± 0.01	0.0411 ± 0.0003	54.3198 ± 0.0018	-
0142.01	291.148071	40.669399	13.113	16.9 ± 0.9	87.4 ± 0.3	0.038 ± 0.001	10.947 ± 0.036	6
0250.01	284.940979	46.566540	15.473	32 ± 2	89.29 ± 0.07	0.051 ± 0.002	12.2827 ± 0.0044	2
0250.02	284.940979	46.566540	15.473	54 ± 6	89.3 ± 0.2	0.047 ± 0.005	17.2509 ± 0.0097	1
0315.01	297.271881	43.333309	12.968	59 ± 5	89.6 ± 0.2	0.029 ± 0.001	35.5812 ± 0.0087	4
0318.01	288.153992	44.068821	12.211	29.1 ± 0.2	89.9 ± 0.2	0.033 ± 0.003	38.5846 ± 0.0049	-
0345.01	286.524811	48.683601	13.340	45 ± 3	89.4 ± 0.2	0.0335 ± 0.0009	29.8851 ± 0.0031	-
0351.01	284.433502	49.305161	13.804	186.2 ± 0.1	89.70 ± 0.001	0.0852 ± 0.0001	331.616 ± 0.025	1
0351.02	284.433502	49.305161	13.804	141 ± 1	90.001 ± 0.001	0.0601 ± 0.0008	210.79 ± 0.41	1
0372.01	299.122437	41.866760	12.391	112 ± 1	89.98 ± 0.08	0.0816 ± 0.0009	125.6287 ± 0.0073	-
0377.01	285.573975	38.400902	13.803	33 ± 2	89.1 ± 0.2	0.078 ± 0.001	19.245 ± 0.023	12
0377.02	285.573975	38.400902	13.803	55 ± 6	89.3 ± 0.2	0.076 ± 0.003	38.95 ± 0.11	2
0410.01	292.248016	40.696049	14.454	33 ± 6	89.0 ± 0.9	0.065 ± 0.007	7.2165 ± 0.0018	6
0448.02	297.070160	40.868790	14.902	45 ± 10	88.9 ± 0.6	0.05 ± 0.01	43.587 ± 0.022	9
0456.01	287.773560	42.869282	14.619	20.4 ± 0.7	88.35 ± 0.07	0.034 ± 0.001	13.699 ± 0.012	3
0464.01	293.747101	45.107220	14.361	75.0 ± 0.3	89.95 ± 0.01	0.0677 ± 0.0008	58.3619 ± 0.0023	-
0523.01	286.047119	45.053211	15.000	45 ± 5	88.9 ± 0.2	0.063 ± 0.003	49.4112 ± 0.0082	1
0525.01	300.907776	45.457870	14.539	20 ± 2	87.3 ± 0.3	0.05 ± 0.01	11.5300 ± 0.0093	4
0528.02	287.101105	46.896481	14.598	102 ± 9	89.6 ± 0.1	0.031 ± 0.002	96.676 ± 0.010	-
0620.01	296.479767	49.937679	14.669	62.7 ± 0.4	89.90 ± 0.02	0.074 ± 0.001	45.1552 ± 0.0028	1
0620.02	296.479767	49.937679	14.669	127.2 ± 0.6	89.98 ± 0.01	0.1017 ± 0.0009	130.1783 ± 0.0058	-
0638.01	295.559418	40.236271	13.595	36.1 ± 0.3	89.65 ± 0.06	0.032 ± 0.001	23.6415 ± 0.0069	2
0738.01	298.348328	47.491230	15.282	27 ± 4	88.79 ± 0.07	0.037 ± 0.003	10.338 ± 0.015	4
0738.02	298.348328	47.491230	15.282	24 ± 2	88.33 ± 0.05	0.034 ± 0.005	13.286 ± 0.019	-
0757.02	286.999481	48.375790	15.841	68 ± 2	89.73 ± 0.07	0.046 ± 0.003	41.196 ± 0.011	-
0759.01	285.718536	48.504849	15.082	37 ± 4	88.8 ± 0.3	0.044 ± 0.003	32.628 ± 0.017	3
0760.01	292.167053	48.727589	15.263	12.2 ± 0.4	86.0 ± 0.2	0.106 ± 0.003	4.9592 ± 0.0012	7
0806.01	285.283630	38.947281	15.403	124 ± 7	89.84 ± 0.09	0.099 ± 0.001	143.200 ± 0.059	3
0806.02	285.283630	38.947281	15.403	75 ± 3	89.9 ± 0.1	0.136 ± 0.003	60.3258 ± 0.0062	4
0829.03	290.461761	40.562462	15.386	37 ± 3	88.7 ± 0.1	0.033 ± 0.003	38.557 ± 0.024	-
0841.01	292.236755	41.085880	15.855	31.3 ± 0.9	89.21 ± 0.07	0.054 ± 0.004	15.334 ± 0.011	1
0841.02	292.236755	41.085880	15.855	39 ± 5	88.9 ± 0.3	0.08 ± 0.01	31.3304 ± 0.0077	3
0854.01	289.508484	41.812119	15.849	89 ± 5	89.75 ± 0.05	0.041 ± 0.002	56.052 ± 0.021	1
0869.02	291.638977	42.436321	15.599	57 ± 2	89.64 ± 0.08	0.037 ± 0.001	36.277 ± 0.027	1
0880.01	292.873383	42.966141	15.158	36 ± 5	88.7 ± 0.4	0.045 ± 0.006	26.4435 ± 0.0097	1
0880.02	292.873383	42.966141	15.158	51 ± 6	89.3 ± 0.2	0.061 ± 0.002	51.537 ± 0.021	7
0886.01	294.773926	43.056301	15.847	8.9 ± 0.4	83.7 ± 0.1	0.07 ± 0.02	8.009 ± 0.015	1
0902.01	287.852386	43.897991	15.754	85 ± 7	89.6 ± 0.1	0.089 ± 0.002	83.927 ± 0.016	7
0918.01	283.977509	44.811562	15.011	51.6 ± 0.2	89.93 ± 0.02	0.116 ± 0.002	39.6432 ± 0.0016	3
0935.01	294.023010	45.853081	15.237	30.9 ± 0.5	89.5 ± 0.1	0.042 ± 0.001	20.860 ± 0.011	1
0935.02	294.023010	45.853081	15.237	40 ± 3	89.0 ± 0.2	0.042 ± 0.002	42.6334 ± 0.0081	-
0935.03	294.023010	45.853081	15.237	52 ± 7	89.1 ± 0.3	0.034 ± 0.002	87.647 ± 0.019	-
0984.01	291.048798	36.839882	11.631	20.6 ± 0.7	88.8 ± 0.1	0.030 ± 0.001	4.2888 ± 0.0031	8
1199.01	293.743927	38.939281	14.887	72 ± 2	89.77 ± 0.08	0.030 ± 0.002	53.526 ± 0.021	-
1271.01	294.265503	44.794300	13.632	105 ± 3	89.64 ± 0.02	0.0693 ± 0.0005	161.98 ± 0.16	4
1353.01	297.465332	42.882839	13.956	112 ± 3	89.85 ± 0.07	0.105 ± 0.001	125.8648 ± 0.0029	7
1366.01	286.358063	42.406509	15.368	29 ± 1	88.9 ± 0.1	0.031 ± 0.003	19.256 ± 0.019	1
1366.02	286.358063	42.406509	15.368	47 ± 12	88.7 ± 0.5	0.05 ± 0.02	54.156 ± 0.021	-
1426.01	283.209167	48.777641	14.232	48.3 ± 0.6	89.67 ± 0.09	0.029 ± 0.001	38.868 ± 0.011	-
1426.02	283.209167	48.777641	14.232	93 ± 11	89.6 ± 0.2	0.065 ± 0.002	74.927 ± 0.011	1
1426.03	283.209167	48.777641	14.232	131 ± 8	89.56 ± 0.05	0.12 ± 0.03	150.025 ± 0.013	-
1429.01	292.351501	48.511082	15.531	114 ± 21	89.6 ± 0.2	0.051 ± 0.003	205.914 ± 0.021	-
1474.01	295.417877	51.184761	13.005	50.4 ± 0.7	88.69 ± 0.05	0.25 ± 0.03	69.721 ± 0.032	2
1573.01	296.846161	40.138611	14.373	59.4 ± 0.9	89.80 ± 0.06	0.045 ± 0.001	24.8093 ± 0.0058	6
1574.01	297.916870	46.965130	14.600	60 ± 10	89.3 ± 0.2	0.067 ± 0.003	114.7356 ± 0.0079	-
1574.02	297.916870	46.965130	14.600	48 ± 7	88.9 ± 0.2	0.036 ± 0.001	191.29 ± 0.17	-
1873.01	295.809296	40.008511	15.674	63.9 ± 0.4	89.90 ± 0.02	0.045 ± 0.002	71.3106 ± 0.0087	-
2672.01	296.132812	48.977402	11.921	80 ± 12	89.5 ± 0.2	0.051 ± 0.003	88.508 ± 0.013	-
2672.02	296.132812	48.977402	11.921	72.2 ± 0.3	89.92 ± 0.01	0.0303 ± 0.0009	42.9933 ± 0.0042	-

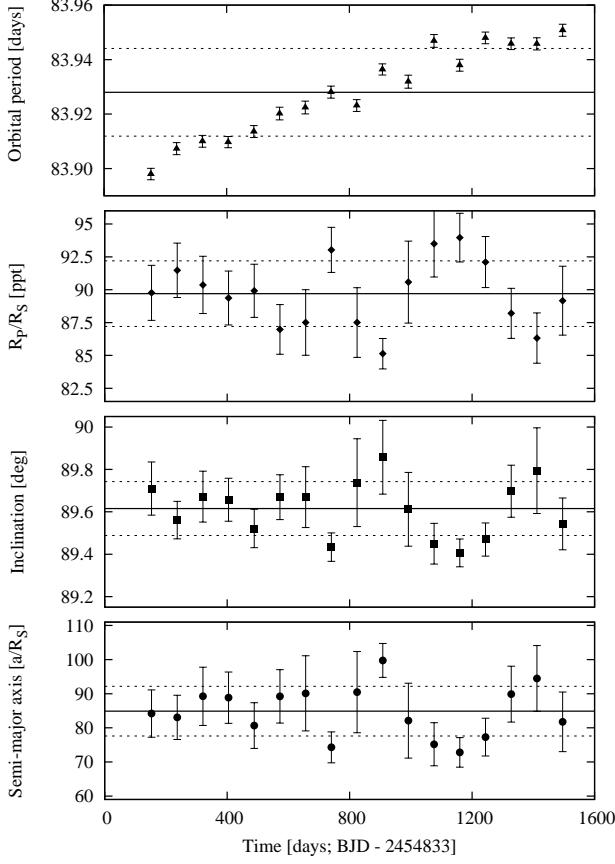


Fig. 4: Time-dependent change of the transit parameters of KOI-0902.01. From top to bottom the orbital period in days in triangles, the planet-to-star radius ratio, R_p/R_s in diamonds, the orbital inclination in squares, and the semi-major axis in stellar radii, a/R_s . Horizontal continuous and dashed lines show mean and standard deviations of the system parameters, respectively. Individual errors are given at $1-\sigma$ level.

prises a primary transit times a detrending component. Thus, to compute TTVs we carry out a more refined detrending of the light curves rather than just a time-dependent polynomial. For the detrending model we consider a linear combination of seeing, airmass, (x,y) centroid positions of the target and of the reference stars, integrated counts over the selected photometric aperture and the (x,y) centroid positions of the master flat field and the master dark frames, when available, and integrated sky counts for the selected sky ring (see e.g., Kundurthy et al. 2013; Becker et al. 2013, for a similar approach in the detrending strategy). Due to the nature of the data the exact time at which the mid-transits will occur are in principle unknown, or known but with a given certainty. Some photometric observations could actually have been taken outside the primary transit occurrence. As a consequence, we have to be extremely careful not to over-fit our data. In order to choose a sufficiently large number of fitting parameters we take into consideration the joint minimization of four statistical indicators: the reduced- χ^2 statistic, χ^2_{red} , the Bayesian Information Criterion, $BIC = \chi^2 + k \ln(Q)$, the standard deviation of the residual light curves enlarged by the number of fitting parameters, $\sigma_{res} \times k$, and the Cash statistic (Cash 1979), $Cash = 2 \sum_{i=1}^Q M_i - D_i * \ln(M_i)$, being M the model and D the data. For the BIC, k is the number of fitting parameters,

and χ^2 is computed from the residuals, obtained by subtracting to the synthetic data the best-fit model. For the BIC and Cash, Q is the number of data points per light curve. The full detrending model, DM, has the following expression:

$$DM(t) = c_0 + c_1 \cdot \hat{\chi} + c_2 \cdot \hat{S} + \sum_{i=1}^{N+1} bg_i \cdot BG_i + fc_i \cdot FC_i + dk_i \cdot DK_i + x_i \cdot X_i + y_i \cdot Y_i \quad (4)$$

Here, $N+1$ denotes the total number of target and reference stars, \hat{S} and $\hat{\chi}$ correspond to seeing and airmass, respectively. X_i and Y_i are the (x,y) centroid positions. FC_i and DK_i are the integrated flat and dark counts in the chosen aperture, respectively, and BG_i correspond to the background counts. The coefficients of the detrending model are c_0, c_1, c_2 , and bg_i, fc_i, dk_i and x_i, y_i , with $i = 1, N+1$. Using a linear combination of these components simplifies the computation of the detrending coefficients that accompany them by means of simple inversion techniques. Rather than using the full detrending model to clean the data from systematics and potentially over-fit the data, we evaluate sub-models of it (this is, a linear combination of some of the detrending components). Typical detrending functions would have the following expression:

$$\begin{aligned} DM_0 &= c_0, \\ DM_1 &= c_0 + c_1 \hat{\chi}, \\ DM_2 &= c_0 + c_1 \hat{\chi} + c_2 \hat{S}, \\ DM_3 &= c_0 + c_2 \hat{S}, \\ DM_4 &= c_0 + \sum_{i=1}^{N+1} bg_i \cdot BG_i, \\ DM_5 &= c_0 + c_1 \hat{\chi} + \sum_{i=1}^{N+1} bg_i \cdot BG_i, \\ &\dots \\ DM_{14} &= c_0 + c_1 \hat{\chi} + c_2 \hat{S} + \sum_{i=1}^{N+1} bg_i \cdot BG_i + x_i \cdot X_i + y_i \cdot Y_i. \\ &\dots \end{aligned} \quad (5)$$

DIP²OL considers a total of 56 sub-models, depending on the availability of calibrations. Usually, the noise in the data is correlated with airmass, (x,y) centroid positions and integrated flat counts, while the dependency with seeing strongly depends on the photometric quality and stability of the particular night. Therefore, these 56 sub-models are constructed solely from how we think the systematics impact the data. Although all possible combinations should be tested, this is computationally expensive, specially considering that a differential light curve can be constructed averaging 20-30 reference stars (i.e., $N = 20-30$).

To determine the detrending sub-model best matching the residual noise in the data, we first create an array of trial T_0 's around the predicted mid-transit time, covering the $\pm T_{dur}$ space and respecting the cadence of the observations. This takes care of the uncertainty in the knowledge of the mid-transit times, since typical errors in the predictions of transits with large TTVs can increase up to 40-50 minutes, in some cases even more. For each one of these trial T_0 's and each one of the sub-models we compute the previously mentioned four statistics. In principle, if a given trial T_0 is close to the true mid-transit time, then around

this T_0 all the sub-models should minimize the four statistics. To illustrate this, Figure 5, *top*, shows how the BIC changes as a function of the trial T_0 , for all the possible sub-models (28 in this case, since dark frames were unavailable). For this example, we analyzed the transit photometry of KOI-0760.01 taken with the 2.5 m Nordic Optical Telescope. Color-coded are the number of detrending components. Figure 5, *bottom*, shows the dependency of the BIC with the sub-models (i.e., detrending models, DM). The numbers on the abscissa are in concordance with the indices in Eq. 5. Color-coded are the trial T_0 's. For this data set, the BIC minimizes at DM₂. As a consequence, the data do not correlate with the integrated flat counts, nor the centroid position. This is actually what we expect, since the Nordic Optical Telescope has an outstanding guiding system that can keep stars within the same pixels for hours.

Then, we make use of the minimization of the time-averaged statistics (that is, the statistics averaged within each one of the T_0 's) to determine the starting value of the mid-transit time that will be used in our posterior transit fitting (see Figure 6). This is a more robust approach than simply computing the absolute minimum value of the statistics, since these could be produced by chance. Finally, with this mid-transit time fixed we re-compute the transit model and re-iterate over all the detrending models to choose the one that minimizes the averaged statistics.

For the transit fitting instance we use a quadratic limb darkening law with quadratic limb darkening values computed as described in von Essen et al. (2013), for the filter band matching the one used during the observations and for the stellar fundamental parameters closely matching the ones of the KOIs. Rather than considering the orbital period, the inclination, the semi-major axis and the planet-to-star radius ratio as fixed parameters to the values given by the NASA Exoplanet Archive or the values derived in Table 2, we use a Gaussian probability distribution which mean and standard deviation equals the values obtained in Section 4.1, and we fit all of them simultaneously to the detrending model and the mid-transit time. The inclination, semi-major axis and planet-to-star radius ratio are fitted only if the light curves show complete transit coverage. If not, we consider them as fixed to the values reported in Table 2, and we fit only the mid-transit time. At each MCMC step the transit parameters change. Therefore, for each iteration we compute the detrending coefficients with the previously mentioned inversion technique. To fit KOINet's ground-based data we produce 5×10^6 repetitions of the MCMC chains, we discard the first 20%, and we compute the mean and standard deviation ($1-\sigma$) of the posterior distributions of the parameters as best-fit values and uncertainties, respectively. To check for the convergence of the chains, we divide the remaining 80% in four, and we compute mean and standard deviations of the priors within each 20%. We consider that the chains converged if all the values are consistent within $1-\sigma$ errors. Finally, we visually inspect the posterior distributions and their correlations.

To provide reliable error bars on the timing measurements we evaluate to what extent our photometric data are affected by correlated noise. To this end, following Carter & Winn (2009) we compute residual light curves by dividing our photometric data by the best-fit transit and detrending models. From the residuals, we compute the β factors as specified in von Essen et al. (2013). Here, we divide each residual light curve into M bins of N averaged data points. If the data are free of correlated noise, then the noise within the residual light curves should follow the expectation of independent random numbers:

$$\hat{\sigma}_N = \sigma_1 N^{-1/2} [M/(M-1)]^{1/2}. \quad (6)$$

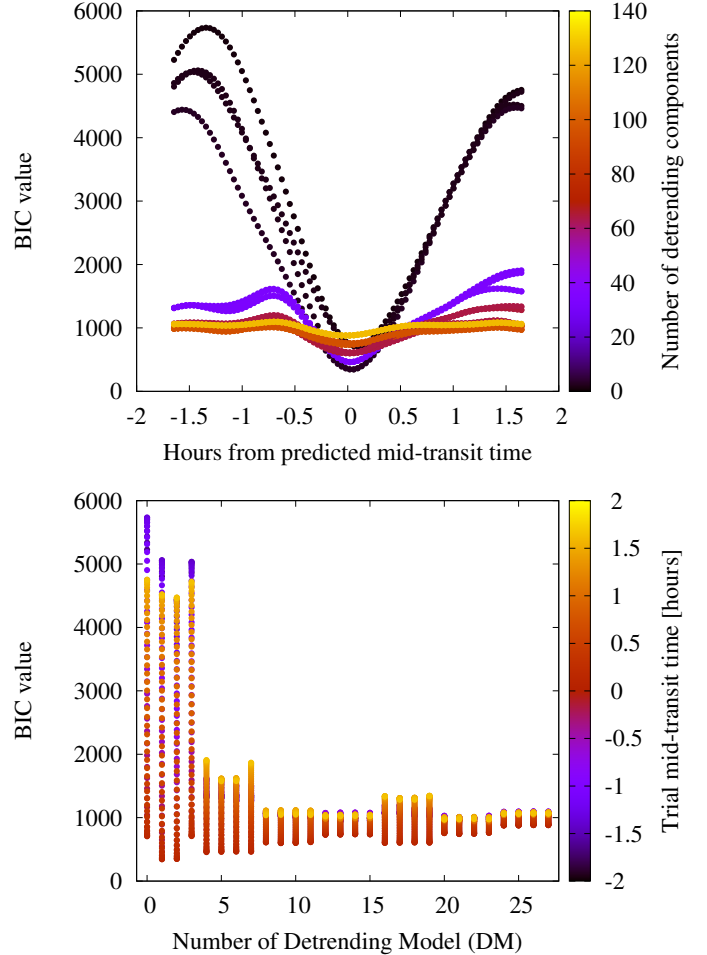


Fig. 5: *Top*: BIC values as a function of trial mid-transit times. Color-coded are the number of detrending components for each one of the detrending models (sub-models). *Bottom*: BIC values as a function of the detrending model, DM. Numbers are in agreement with the labels on Eq. 5. Color-coded are the trial T_0 's.

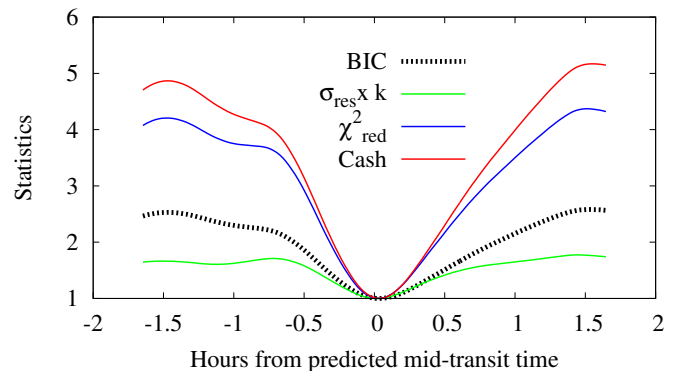


Fig. 6: The four statistics used to assess the number of detrending components and the starting mid-transit time, obtained analyzing KOI-0760 data. Their values have been normalized and scaled to allow for visual comparison. The thick dashed black line corresponds to the time-averaged BIC statistics, as shown in the top panel of Figure 5.

Here, σ_1 corresponds to the scatter of the unbinned residuals, and σ_N to the variance of the binned data:

$$\sigma_N = \sqrt{\frac{1}{M} \sum_{i=1}^M (\langle \hat{\mu}_i \rangle - \hat{\mu}_i)^2}, \quad (7)$$

In the equation, the mean value of the residuals per bin is given by $\hat{\mu}_i$, and $\langle \hat{\mu}_i \rangle$ is the mean value of the means. In the presence of correlated noise, σ_N should differ by the factor β_N from σ_1 . Therefore, we compute β by averaging the β_N 's obtained over time bins close to the duration of ingress, which is in turn computed from the previously determined best-fit transit parameters. In particular, we consider time bins as large as 0.8, 0.9, 1, 1.1, and 1.2 times the duration of ingress. If β is larger than 1, we enlarge the photometric error bars by this value, and we carry out the MCMC fitting in the exact same fashion as previously explained. We conclude by visually inspecting the data, the detrending model, and the best-fit transit model.

5. KOINet's achieved milestones

5.1. Photometric data presented in this work

Here we present seven new primary transit observations of KOI-0760.01, KOI-0410.01, KOI-0525.01 and KOI-0902.01. These were taken between May, 2014 and July, 2015. Table 3 shows the basic photometric characteristics of the data, such as the photometric precision, the cadence and number of data points per light curve, the transit coverage and the dates at which the KOIs were observed. The last column of Table 3 shows their corresponding mid-transit times, along with 1- σ uncertainties. The KOIs presented in this work were chosen to exemplify the need for a network such as KOINet, as described in the following sections.

We would like to emphasize that the purpose of this paper is to show the potential of KOINet. Therefore, we present the TTV observations, together with preliminary models. For individual cases (e.g., KOI-0410.01) a more in-depth analysis is also given.

Most of the KOIs that are members of KOINet's follow-up are in wide orbits. In particular, the average orbital period of these KOIs is around 65 days, while the largest orbit corresponds to 335 days. As a consequence, most of the transits last several hours, with an average value of about 6 ± 3 hours. Thus, it is challenging to cover the full transit from the ground. Normally, incomplete transit coverage has a large impact in the determination of the mid-transit times (see e.g. Winn et al. 2008; Gibson et al. 2009). However, in our case this is alleviated by the prior knowledge of the orbital parameters given by Kepler photometry. While long cadence Kepler data were obtained averaging images each 30 minutes, the collected ground-based observations have a cadence between some seconds to a few minutes. Although our Earth's atmosphere and typical ground-based instrumental imperfections considerably decrease the photometric precision when compared to Kepler data, we gain in sampling rate and, thus, in timing precision, given the prior knowledge of the transit parameters.

5.2. Timing precision: KOI-0760.01

Figure 10(a), shows a primary transit of KOI-0760.01 and its corresponding TTVs. The target is a Neptune-sized planet candidate in a ~ 5 day orbit, showing TTVs of small amplitude (~ 140 seconds). The TTV period is of around 3.5 years and, as a consequence, has been roughly covered by the Kepler data. The

TTVs show also a scatter of ~ 2 minutes. To include a KOI into KOINet's follow-up list, it has to fulfill specific conditions. One of them is to present TTVs larger than (or about) two minutes. KOI-0760.01 is close to the lower end of this limit. Compared with Kepler averaged errors in the mid-transit times (~ 80 seconds) ground-based data collected by KOINet delivered a timing precision of the same quality. The left panel of Figure 10(a), shows a detrended transit light curve in green, the best fit model in black continuous line, and the raw data and detrended model in blue points and black continuous line, respectively. For a better visualization, these were arbitrarily shifted. The figure on the right shows Kepler and ground-based TTVs in red diamonds. Red and green-shaded areas indicate Kepler coverage and the ground-based, 2014 observing season, respectively.

5.3. Photometric precision: KOI-0525.01

Another strong limit set by the nature of ground-based observations is given by the transit depth. For Kepler targets with TTVs, this is aggravated by the faintness of the stars, the length of the transits, and the uncertainty of the transit occurrence. Before starting the observing seasons we set an ambitious lower limit in the transit depth of ~ 1 ppt, with the final cut given by the TTV amplitude and the transit duration. To maximize the transit detection, we assigned these transits to the largest telescopes. One successful example of our observing strategy is given by KOI-0525.01. The KOI is labeled as an exoplanet candidate, and beside the small (~ 1 ppt) transit depth, it has an orbital period of ~ 11.5 days, and a transit duration of ~ 2.25 hours, facilitating observations of complete transits from the ground. The TTV periodicity shown by Kepler data is longer than four years, so our observations will help to set constraints on the nature of the KOI. Figure 10(b), shows the ground-based light curve obtained with the ARC 3.5m telescope. We detected the transit and a turnover in the TTVs of KOI-0525.01, shown in the right side of Figure 10(b). With the addition of the holographic diffuser on the new ARCTIC imager on the ARC 3.5 m Telescope at Apache Point Observatory, we may be able to achieve even higher photometric precision in future observations (Stefansson et al. 2017).

5.4. Relevance for ground-based follow-ups: KOI-0902.01

When the TTV periodicity is not fully sampled, it can occur that the quickly increasing separation between the two most likely scenarios (sinusoidal and parabolic predictions) prevents us from finding future transits of these KOIs. For some KOIs, like KOI-0410.01 (see next Section) the difference between these two extreme scenarios is of the order of a couple minutes and will be well contained below some hours in the upcoming years. However, for some other KOIs the current difference is larger than the duration of an observing night. Therefore, if follow-up campaigns are not carried out in time it will be extremely expensive to detect the transits of these planet candidates again. A clear example of this is given by KOI-0902.01. The exoplanet candidate is in an ~ 84 days orbit, and the transit duration is of ~ 6.7 hours, making the full observation of a single transit quite challenging from only one observing site. Figure 10(c), shows one of the transits observed by the IAC 0.8m telescope. The transit ($\Delta F \sim 1\%$) has been clearly detected by KOINet. On the right panel, the TTVs of Kepler data plus the ground-based detected mid-time can be seen.

Table 3: Most relevant parameters obtained from our observations. From left to right: the date corresponding to the beginning of the local night in years, months and days (yyyy.mm.dd), the name of the observed KOI, the telescope performing the observations, the standard deviation of the residual light curves in parts-per-thousand (ppt), σ_{res} , the number of data points per light curve, N, the average cadence in seconds, CAD, the total observing time, T_{tot} , in hours, and the airmass range, $\chi_{min,max}$, showing minimum and maximum values, respectively, the transit coverage, TC (a description of the transit coding is detailed in the footnote of this table) and the derived mid-transit times, in BJD_{TDB} .

Date yyyy.mm.dd	Telescope	Name	σ_{res} (ppt)	N	CAD (sec)	T_{tot} (hours)	$\chi_{min,max}$	TC	TTVs $\pm 1-\sigma$ BJD_{TDB}
2014.06.24	IAC 0.8m	KOI-0902.01	1.8	114	210	6.67	1.03,1.63	-BEO	2456832.43925 \pm 0.0063
2014.08.28	ARC 3.5m	KOI-0525.01	0.7	135	60	2.26	1.02,1.06	OIBE-	2456897.71506 \pm 0.0045
2014.10.03	NOT 2.5m	KOI-0760.01	1.4	302	59	5.00	1.07,2.50	OIBEO	2456934.43353 \pm 0.0010
2014.10.12	NOT 2.5m	KOI-0410.01	1.0	178	81	4.01	1.06,2.29	OIBEO	2456943.41142 \pm 0.0018
2014.11.03	YO 2.4m	KOI-0410.01	1.4	128	110	3.91	1.10,2.78	OIBEO	2456965.06535 \pm 0.0020
2015.07.06	CAHA 2.2m	KOI-0410.01	3.7	670	41	7.75	1.00,1.50	OIBEO	2457210.43420 \pm 0.0031
2015.07.06	NOT 2.5m	KOI-0410.01	0.8	142	95	3.77	1.02,1.51	-IBEO	2457210.43652 \pm 0.0022

Notes. Acronyms for the telescopes are as specified in Section 2.3. The letter code specifying the transit coverage during each observation is the following: O: out of transit, before ingress. I: ingress. B: flat bottom. E: egress. O: out of transit, after egress.

5.5. Turn-over of TTVs: KOI-0410.01

In the NASA Exoplanet Archive, more specifically within the Data Validation Reports (DV), KOI-0410.01 has been identified as a false positive. Most of the evidence in favor of this status is based upon the V-shape of its transits. The flux drops take place each ~ 7.2 days, and the transit depth is about 5 ppt. During 2014 and 2015 we have observed four transits of KOI-0410.01. The characteristics of the data are presented in Table 3. The combination of Kepler and ground-based TTVs, shown in Figure 10(d), reveal a turn-over in their mid-times. This, together with the assigned status, motivates a more detailed study to shed some light into the nature of the system.

To begin with, in the DV report a source of 18.4 Kepler magnitudes has been detected, approximately nine arcseconds away from the nominal position of KOI-0410. Therefore, it could be possible that a background eclipsing binary could be causing the observed flux drops, there. For well spatially resolved ground-based observations, 9 arcseconds corresponds to several dozens of pixels. To identify the source, we combined all the observations of our best (sharpest) night. Once the mentioned source was located, we carried out the usual differential photometry, choosing different apertures centered on KOI-0410, both including and excluding the source. As expected, the increase or decrease in aperture (from 0.9 to 10 arcseconds) changed the overall photometric accuracy of the differential light curves. However, it did not change the shape or depth of the transit. Therefore, as also observed by Bouchy et al. (2011) it is unlikely that the flux drops are caused by a background binary 9 arcseconds away from KOI-0410.

Furthermore, we investigated the case in which the flux drops were caused by a grazing eclipsing binary in a ~ 7.2 days orbit, or two similar stars in a ~ 14.4 -day orbit, eclipsing each other each ~ 7.2 days. In both cases, the radial velocity shifts caused by their mutual orbital motion would create a detectable variability, not observed by Bouchy et al. (2011). These authors observed KOI-0410 at two opportunities, at orbital phases close to 0.5 and 0.75, detecting RV shifts inconsistent with the ones expected to be caused by two orbiting stars. To examine the scenario of two identical stars in more detail, we simulated two identical G-type stars using the PHysics Of Eclipsing Binaries⁶ (PHOEBE Prša et al. 2016) code. We assumed stellar radii consistent with G-type stars, with limb darkening coefficients chosen accord-

ingly and computed as described in von Essen et al. (2013), and we changed the inclination to match both the eclipse duration and depth. On one hand, for an inclination of 74.6 degrees we matched the eclipse depth (~ 5 ppt, 4460.6 ± 17.8 parts per million, as reported in the NASA Exoplanet Archive). However, the eclipse duration exceeds the observed one ($T_{dur} = 1.899$ hours, NASA Exoplanet Archive). On the other hand, decreasing the inclination to 73.8 degrees decreases the eclipse duration considerably (less than 2 hours). Nonetheless, the eclipse depth was smaller than ~ 0.05 ppt (see Figure 7, top). Thus, we could not match both transit depth and duration of KOI-0410.01 to the light curves produced from PHOEBE models. In addition to this, both models predict a variability outside eclipse of about $\sim 1\%$, which would be clearly visible in Kepler data (Figure 7, bottom). After visually inspecting the raw data of the 17 quarters and finding no variability modulated with the mentioned periodicity and amplitude, we believe is unlikely that the flux drop is caused by two identical stars in grazing orbits. In addition, the stars should be in exact circular orbits to not show odd/even timing differences, these in turn not observed in the DV report.

Finally, we investigated another two scenarios: a gravitationally-bound hierarchical triple star system, and a planet-star system. Here we show some initial results assuming a planet-star system. In this case, the simultaneous MCMC transit fitting of ground and space-based data allows for a planet solution. Assuming this, the right panel of Figure 10(d) shows some initial TTV results obtained from the data acquired during the first and second observing seasons, together with Kepler data. As the figure shows, additional data already scheduled for the 2018 observing season will constrain the solutions even further. The TTV fits were carried out with a novel version of TTVFast (Deck et al. 2014) which utilizes an symplectic integrator developed by Hernandez & Bertschinger (2015) and the universal Kepler solver of Wisdom & Hernandez (2015). We computed the TTVs caused by a single, outer perturbing planet near 5:3, 3:2, 2:1, 3:1, and 4:1 period ratios (see Figure 8 and Table 4), starting the solution just interior and just exterior to each resonance with a super-period (Lithwick et al. 2012) corresponding to ≈ 3000 days, following the analysis by Ballard et al. (2011) of Kepler-19. We held the mass-ratio of the transiting planet (KOI-0410.01) to the star fixed at 10^{-5} , while we allowed the initial ephemerides and eccentricity vectors of both planets to vary, as well as the mass-ratio of the perturbing planet. We assumed a plane-parallel configuration, and specified the initial

⁶ <http://phoebe-project.org/>

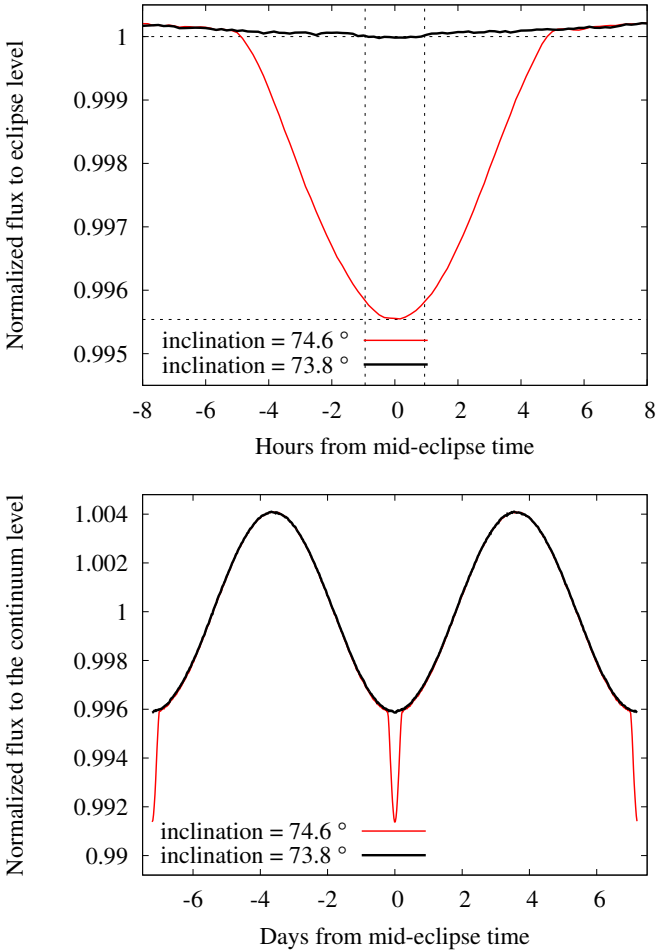


Fig. 7: PHOEBE models for two identical G-type stars in a ~ 14.4 -day orbit, for an inclination of 74.6° in red, and 73.8° in black continuous lines. *Top*: zoom-in around the eclipses. Time is given in hours. Horizontal and vertical dashed lines indicate the transit duration and depth, respectively, for visual inspection. *Bottom*: complete orbits, highlighting the continuum flux variability.

orbital elements at $\text{BJD}_{\text{TDB}} - 2454833 = 130$ days. We optimized the model using a Levenberg-Marquardt solver (Press et al. 1993) with numerically-computed, double-sided derivatives. We found relatively good fits near all of these mean-motion resonances, with χ^2 values ranging from 243 to 290 for 160 degrees of freedom. These chi-square values are uncomfortably large, which may indicate that the timing uncertainties of the planets are underestimated by 20% (in the scenario in which the treatment of correlated noise is not sufficient to account for this noise), or created by an astrophysical source, both equally speculative with the data we currently have. The mass ratios of the perturbing planets for these solutions varied from 10^{-6} to 3×10^{-5} (4), while the eccentricities of both planets are modest, < 0.15 . We leave a more detailed description of these results to future work.

To investigate the gravitationally-bound hierarchical triple star system scenario, we computed the Spectral Energy Distribution (SED) of KOI-0410. For this end, we used all its available colors, taken from the NASA Exoplanet Archive. These were compared to “synthetic colors” which, in turn, were produced from PHOENIX stellar models. In particular, when

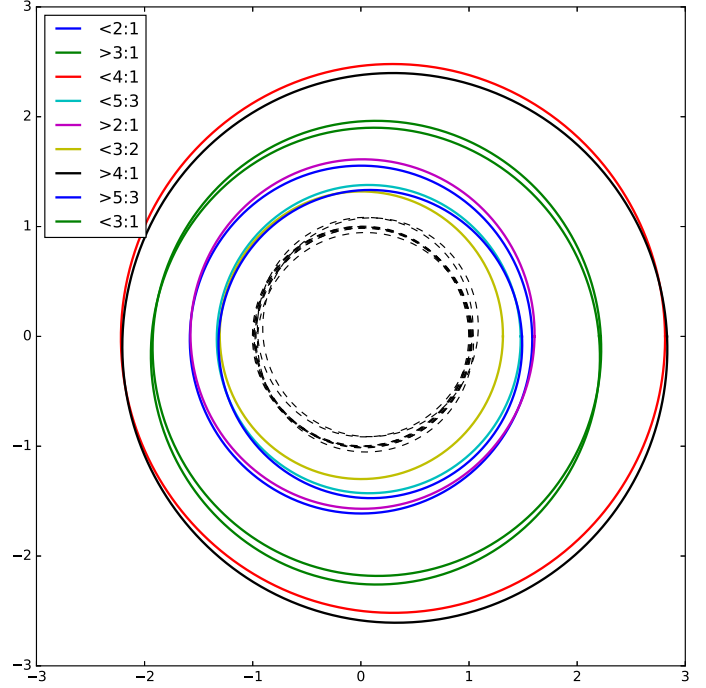


Fig. 8: The shapes of the orbits for each one of the exterior perturber TTV solutions. The dashed lines represent the orbits for the transiting planet in each case. The axis units are in terms of the semi-major axis of the transiting planet. The exact values for the mass and period ratios are specified in Table 4. The solution just interior to 3:2 isn’t plotted due to large χ^2 values.

Table 4: Numerical outcomes for the mass (perturber-to-star) and period (perturber-to-transiting planet) ratios for each one of the exterior perturber TTV solutions.

Ratio	Mass-ratio	Period ratio
$< 2 : 1$	1.87×10^{-5}	1.993
$> 3 : 1$	2.17×10^{-5}	3.009
$< 4 : 1$	1.18×10^{-5}	3.991
$< 5 : 3$	2.06×10^{-6}	1.666
$> 2 : 1$	2.63×10^{-5}	2.007
$< 3 : 2$	1.23×10^{-6}	1.498
$> 4 : 1$	1.23×10^{-5}	4.006
$> 5 : 3$	2.96×10^{-6}	1.667
$< 3 : 1$	2.31×10^{-5}	2.994

producing the synthetic colors we investigated a wide range of stellar parameters, namely $T_{\text{eff}} = 6000, 6100, 6200$ Kelvin, $\log(g) = 4.0, 4.5$, and $[\text{Fe}/\text{H}] = -0.5, 0.0$. If more than one star of similar spectral type would conform the KOI-0410 system, they should be revealed as an excess in the SED, when compared to PHOENIX colors produced from a single star. We find a perfect match between the observed and modeled colors for a star of $T_{\text{eff}} = 6100$ Kelvin, $\log(g) = 4.5$, and $[\text{Fe}/\text{H}] = -0.5$, close to the values of KOI-0410 reported in the bibliography, with the exception of two photometric bands, namely i and z (see Figure 9), which we believe is caused by an incorrect treatment of atmospheric extinction rather than astrophysics). Since all the Sloan measurements do not have uncertainties, during the upcoming 2018 observing season we will re-observe KOI-0410 in these photometric bands. At this point we would like to stress that, for the KOI-0410 system, the data available can not really disentangle

gle between the hierarchical triple star system and the planet-star system, not even considering the TTVs. For example, if the binary system was formed by two M-dwarf stars diluted by a G-type star, then the stellar parameters and the radial velocity measurements would be dominated by the latter, while the ~ 14.4 -day period M-dwarf binary (diluted by the G-dwarf) might explain the Kepler transits. A G-dwarf star orbiting an M-dwarf binary in a ~ 3000 days, eccentric orbit might be sufficient to produce the observed TTVs (Borkovits et al. 2003; Agol et al. 2005), causing an ambiguity with the planet-star scenario. We leave a more detailed examination of this scenario to future work.

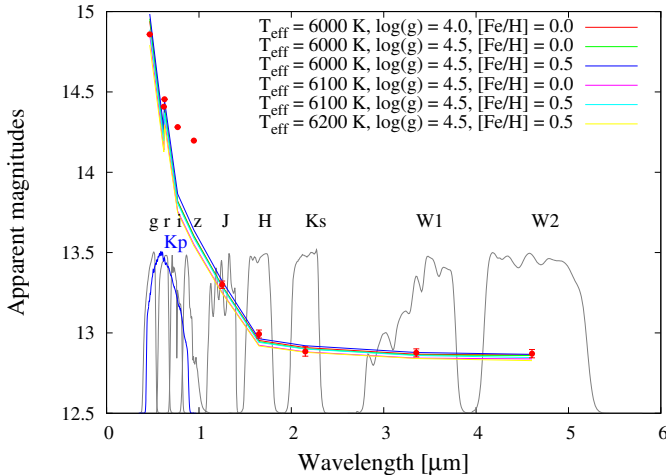


Fig. 9: Spectral energy distribution for KOI-0410. The figure shows apparent magnitudes as a function of wavelength, in μm . Shifted and scaled to match the figure, we have added in gray and blue continuous lines the filter transmission functions. On top of them, their respective names: Sloan g, r, i and z, Kepler band (K_p), 2MASS J, H and Ks, and WISE W1, W2. The first five quantities do not have uncertainties.

6. Conclusions

KOINet is a large collaboration spanning multiple telescopes across the world aimed at achieving a follow-up coverage of KOIs exhibiting TTVs. We have been focusing our instrumental capabilities initially on 60 KOIs that require additional data to complete a proper characterization or confirmation by means of the TTV technique. A complete list of these KOIs with all the relevant parameters has been provided here.

There are several main challenges associated with the KOIs included in this study: the faintness of their host stars, their shallowness and their long duration. KOINet presents two fundamental advantages: the access to *large telescopes* has allowed us to follow-up KOIs that are faint (~ 13 - $16 K_p$) and present shallow primary transit events (1-10 ppt), minimizing observational biases. The advantage of ground-based observations is the possibility to acquire short-cadence data, of fundamental relevance for the determination of the mid-transit times. Since the TTVs have already been detected by Kepler and most of the systems show a TTV amplitude of several minutes, detecting such offsets has been a straightforward task. The access to *large longitudinal coverage* allowed us to have access to several transit occurrences. In addition, since the transit duration grows with the orbital period, for some of the KOIs the transit duration is

longer than the astronomical night at a given site. Therefore, more than one site is required to fully observe the transit events. With the observations collected during the 2014 and 2015 observing seasons we have succeed with our timing precision requirements, we have added new data improving the coverage of the TTV curves of systems where Kepler did not register the interaction time fully, and we have built a platform that can observe almost anywhere from the Northern hemisphere. Although deriving planetary masses from transit timing observations for more planets to populate the mass-radius-diagram is an ambitious milestone, the work presented here shows we are on the right track.

Acknowledgements. Funding for the Stellar Astrophysics Centre is provided by The Danish National Research Foundation (Grant DNRF106). This research has made use of the NASA Exoplanet Archive, which is operated by the California Institute of Technology, under contract with the National Aeronautics and Space Administration under the Exoplanet Exploration Program. E.A. acknowledges support from NASA Grants NNX13A124G, NNX13AF62G, from National Science Foundation (NSF) grant AST-1615315, and from NASA Astrobiology Institutes Virtual Planetary Laboratory, supported by NASA under cooperative agreement NNH05ZDA001C. S.W. acknowledges support from the Research Council of Norway's grant 188910 to finance service observing at the NOT, and support for International Team 265 (Magnetic Activity of M-type Dwarf Stars and the Influence on Habitable Extra-solar Planets) funded by the International Space Science Institute (ISSI) in Bern, Switzerland. J.F. acknowledges funding from the German Research Foundation (DFG) through grant DR 281/30-1. Based on observations made with the Nordic Optical Telescope, operated by the Nordic Optical Telescope Scientific Association at the Observatorio del Roque de los Muchachos, La Palma, Spain, of the Instituto de Astrofísica de Canarias. The data presented here were obtained in part with ALFOSC, which is provided by the Instituto de Astrofísica de Andalucía (IAA) under a joint agreement with the University of Copenhagen and NOTSA. Based on observations obtained with the Apache Point Observatory 3.5-meter telescope, which is owned and operated by the Astrophysical Research Consortium. Based on observations collected at the German-Spanish Astronomical Center, Calar Alto, jointly operated by the Max-Planck-Institut für Astronomie Heidelberg and the Instituto de Astrofísica de Andalucía (CSIC). This work was supported in part by the Ministry of Education and Science (the basic part of the State assignment, RK no. AAAA-A17-117030310283-7) and by the Act no. 211 of the Government of the Russian Federation, agreement no. 02.A03.21.0006. E.H. and I.R. acknowledge support by the Spanish Ministry of Economy and Competitiveness (MINECO) and the Fondo Europeo de Desarrollo Regional (FEDER) through grant ESP2016-80435-C2-1-R, as well as the support of the Generalitat de Catalunya/CERCA programme. E.P., G.T. and Š.M. acknowledges support from the Research Council of Lithuania (LMT) through grant LAT-08/2016. C.D.C. is supported by the Erasmus Mundus Joint Doctorate Program by the grant number 2014-0707 from the EACEA of the European Commission. S.E. acknowledges support from the Russian Science Foundation grant No. 14-50-00043 for conducting photometric observations of exoplanets of Kepler's mission. S.I. acknowledges Russian Foundation for Basic Research (project No. 17-02-00542) for support in the processing of the observations. K.P. acknowledges support from the UK Science and Technology Facilities Council through STFC grant ST/P000312/1. H.J.D. acknowledges support by grant ESP2015-65712-C5-4-R of the Spanish Secretary of State for R&D&I (MINECO). KOINet thanks the telescope operators for their valuable help during some of the observing campaigns at the IAC80 telescope. The IAC80 telescope is operated on the island of Tenerife by the Instituto de Astrofísica de Canarias in the Spanish Observatorio del Teide. C.v.E. thanks the invaluable help and contribution of all the telescope operators involved in this work.

References

- Agol, E., Steffen, J., Sari, R., & Clarkson, W. 2005, MNRAS, 359, 567
- Ballard, S., Fabrycky, D., Fressin, F., et al. 2011, ApJ, 743, 200
- Barros, S. C. C., Almenara, J. M., Demangeon, O., et al. 2015, MNRAS, 454, 4267
- Barros, S. C. C., Diaz, R. F., Santerne, A., et al. 2013, ArXiv e-prints
- Barros, S. C. C., Díaz, R. F., Santerne, A., et al. 2014, A&A, 561, L1
- Becker, A. C., Kundurthy, P., Agol, E., et al. 2013, ApJ, 764, L17
- Becker, J. C., Vanderburg, A., Adams, F. C., Rappaport, S. A., & Schwengeler, H. M. 2015, ApJ, 812, L18
- Borkovits, T., Érdi, B., Forgács-Dajka, E., & Kovács, T. 2003, A&A, 398, 1091
- Borucki, W. J., Koch, D., Basri, G., et al. 2010, Science, 327, 977
- Bouchy, F., Bonomo, A. S., Santerne, A., et al. 2011, A&A, 533, A83

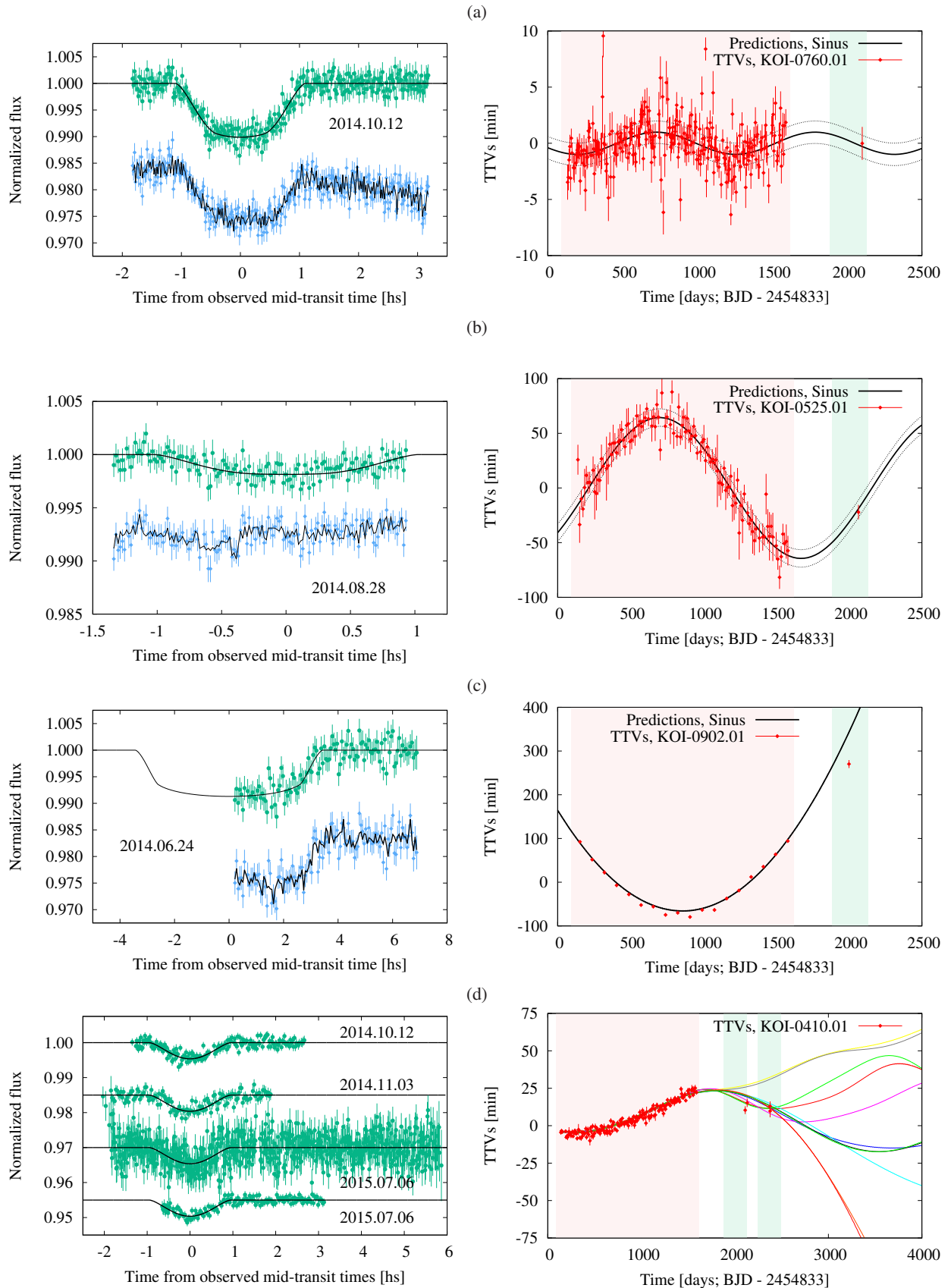


Fig. 10: *Left figures:* From top to bottom, transit observations of KOI-0760.01, KOI-0525.01, KOI-0902.01, and KOI-0410.01. The data are plotted in hours with respect to their best-fit mid-transit times. In all cases green circles show detrended data, along with the best-fit model as black continuous lines. For the first three cases only, the raw data are shown as blue diamonds, plus the detrending times transit models are also overplotted as black lines, shifted down for a better visual comparison, to exemplify our detrending strategy. *Right:* Kepler and ground-based TTVs in red diamonds, for the KOIs displayed on the left. Continuous and dashed black and color lines indicate the predictions and uncertainties, respectively. While the red shaded area represents Kepler observing time, the green shaded areas represent the 2014 and 2015 observing seasons (March til October).

- Carter, J. A., Agol, E., Chaplin, W. J., et al. 2012, *Science*, 337, 556
- Carter, J. A. & Winn, J. N. 2009, *ApJ*, 704, 51
- Cash, W. 1979, *ApJ*, 228, 939
- Claret, A., Hauschildt, P. H., & Witte, S. 2013, *A&A*, 552, A16
- Cochran, W. D., Fabrycky, D. C., Torres, G., et al. 2011, *ApJS*, 197, 7
- Collins, K. A., Kielkopf, J. F., & Stassun, K. G. 2017, *AJ*, 153, 78
- Deck, K. M., Agol, E., Holman, M. J., & Nesvorný, D. 2014, *ApJ*, 787, 132
- Eastman, J., Siverd, R., & Gaudi, B. S. 2010, *PASP*, 122, 935
- Fabrycky, D. C., Ford, E. B., Steffen, J. H., et al. 2012, *ApJ*, 750, 114
- Fabrycky, D. C., Lissauer, J. J., Ragozzine, D., et al. 2014, *ApJ*, 790, 146
- Fang, J. & Margot, J.-L. 2012, *ApJ*, 761, 92
- Ford, E. B., Fabrycky, D. C., Steffen, J. H., et al. 2012a, *ApJ*, 750, 113
- Ford, E. B. & Holman, M. J. 2007, *ApJ*, 664, L51
- Ford, E. B., Ragozzine, D., Rowe, J. F., et al. 2012b, *ApJ*, 756, 185
- Fukui, A., Narita, N., Kawashima, Y., et al. 2016, *ApJ*, 819, 27
- Fukui, A., Narita, N., Tristram, P. J., et al. 2011, *PASJ*, 63, 287
- Gibson, N. P., Pollacco, D., Simpson, E. K., et al. 2009, *ApJ*, 700, 1078
- Gillon, M., Jehin, E., Lederer, S. M., et al. 2016, *Nature*, 533, 221
- Hadden, S. & Lithwick, Y. 2014, *ApJ*, 787, 80
- Hadden, S. & Lithwick, Y. 2017, *AJ*, 154, 5
- Hernandez, D. M. & Bertschinger, E. 2015, *Monthly Notices of the Royal Astronomical Society*, 452, 1934
- Holczer, T., Mazeh, T., Nachmani, G., et al. 2016, *ApJS*, 225, 9
- Holman, M. J., Fabrycky, D. C., Ragozzine, D., et al. 2010, *Science*, 330, 51
- Holman, M. J. & Murray, N. W. 2005, *Science*, 307, 1288
- Howell, S. B. 2006, *Handbook of CCD Astronomy*, ed. R. Ellis, J. Huchra, S. Kahn, G. Rieke, & P. B. Stetson
- Jiang, I.-G., Lai, C.-Y., Savushkin, A., et al. 2016, *AJ*, 151, 17
- Jones, E., Oliphant, T., Peterson, P., et al. 2001, *SciPy: Open source scientific tools for Python*, <http://www.scipy.org>
- Jontof-Hutter, D., Ford, E. B., Rowe, J. F., et al. 2016, *ApJ*, 820, 39
- Jontof-Hutter, D., Rowe, J. F., Lissauer, J. J., Fabrycky, D. C., & Ford, E. B. 2015, *Nature*, 522, 321
- Kipping, D. M. 2010, *MNRAS*, 408, 1758
- Kipping, D. M., Nesvorný, D., Buchhave, L. A., et al. 2014, *ApJ*, 784, 28
- Kjeldsen, H. & Frandsen, S. 1992, *PASP*, 104, 413
- Koch, D. G., Borucki, W. J., Basri, G., et al. 2010, *ApJ*, 713, L79
- Kundurthy, P., Barnes, R., Becker, A. C., et al. 2013, *ApJ*, 770, 36
- Laughlin, G. & Chambers, J. E. 2001, *The Astrophysical Journal*, 551, L109
- Lissauer, J. J., Dawson, R. I., & Tremaine, S. 2014, *Nature*, 513, 336
- Lissauer, J. J., Fabrycky, D. C., Ford, E. B., et al. 2011a, *Nature*, 470, 53
- Lissauer, J. J., Ragozzine, D., Fabrycky, D. C., et al. 2011b, *ApJS*, 197, 8
- Lithwick, Y., Xie, J., & Wu, Y. 2012, *The Astrophysical Journal*, 761, 122
- Maciejewski, G., Dimitrov, D., Neuhäuser, R., et al. 2011, *MNRAS*, 411, 1204
- Maciejewski, G., Dimitrov, D., Seeliger, M., et al. 2013, *A&A*, 551, A108
- Malhotra, R., Black, D., Eck, A., & Jackson, A. 1992, *Nature*, 356, 583
- Mallonn, M., Nascimbeni, V., Weingrill, J., et al. 2015, *A&A*, 583, A138
- Mandel, K. & Agol, E. 2002, *ApJ*, 580, L171
- Mazeh, T., Nachmani, G., Holczer, T., et al. 2013, *ApJS*, 208, 16
- Mislis, D., Mancini, L., Tregloan-Reed, J., et al. 2015, *MNRAS*, 448, 2617
- Mordasini, C., Alibert, Y., Georgy, C., et al. 2012, *A&A*, 547, A112
- Mukadam, A. S., Owen, R., Mannery, E., et al. 2011, *PASP*, 123, 1423
- Nespral, D., Gandolfi, D., Deeg, H. J., et al. 2016, *ArXiv e-prints*
- Nesvorný, D., Kipping, D., Terrell, D., & Feroz, F. 2014, *ApJ*, 790, 31
- Nesvorný, D., Kipping, D., Terrell, D., et al. 2013, *ApJ*, 777, 3
- Nesvorný, D. & Morbidelli, A. 2008, *ApJ*, 688, 636
- Ofir, A., Dreizler, S., Zechmeister, M., & Husser, T.-O. 2014, *A&A*, 561, A103
- Patil, A., Huard, D., & Fonnesbeck, C. J. 2010, *Journal of Statistical Software*, 35, 1
- Peale, S. J. 1993, *The Astronomical Journal*, 105, 1562
- Petrucci, R., Jofré, E., Melita, M., Gómez, M., & Mauas, P. 2015, *MNRAS*, 446, 1389
- Press, W. H., Teukolsky, S. A., Vetterling, W. T., & Flannery, B. P. 1993, *Numerical Recipes in FORTRAN; The Art of Scientific Computing*, 2nd edn. (New York, NY, USA: Cambridge University Press)
- Prša, A., Conroy, K. E., Horvat, M., et al. 2016, *ApJS*, 227, 29
- Raetz, S., Maciejewski, G., Seeliger, M., et al. 2015, *MNRAS*, 451, 4139
- Rasio, F. A., Nicholson, P. D., Shapiro, S. L., & Teukolsky, S. A. 1992, *Nature*, 355, 325
- Rivera, E. J., Laughlin, G., Butler, R. P., et al. 2010, *ApJ*, 719, 890
- Seager, S. 2010, *Exoplanet Atmospheres: Physical Processes*
- Southworth, J., Hinse, T. C., Jørgensen, U. G., et al. 2009, *MNRAS*, 396, 1023
- Steffansson, G., Mahadevan, S., Hebb, L., et al. 2017, *ApJ*, 848, 9
- Steffen, J. H. & Agol, E. 2005, *Monthly Notices of the Royal Astronomical Society: Letters*, 364, L96
- Steffen, J. H., Fabrycky, D. C., Ford, E. B., et al. 2012a, *MNRAS*, 421, 2342
- Steffen, J. H., Ragozzine, D., Fabrycky, D. C., et al. 2012b, *Proceedings of the National Academy of Science*, 109, 7982
- von Essen, C., Cellone, S., Mallonn, M., Tingley, B., & Marcussen, M. 2016, *ArXiv e-prints*
- von Essen, C., Schröter, S., Agol, E., & Schmitt, J. H. M. M. 2013, *A&A*, 555, A92
- Winn, J. N., Holman, M. J., Torres, G., et al. 2008, *ApJ*, 683, 1076
- Wisdom, J. & Hernandez, D. M. 2015, *Monthly Notices of the Royal Astronomical Society*, 453, 3015
- Wolszczan, A. 1994, *Science*, 264, 538
- Xie, J.-W. 2013, *ApJS*, 208, 22
- Xie, J.-W. 2014, *ApJS*, 210, 25
- Young, A. T., Genet, R. M., Boyd, L. J., et al. 1991, *PASP*, 103, 221

¹Stellar Astrophysics Centre, Ny Munkegade 120, 8000, Aarhus, Denmark

²Institut für Astrophysik, Georg-August-Universität Göttingen, Friedrich-Hund-Platz 1, 37077 Göttingen, Germany
e-mail: cessen@phys.au.dk

³Department of Earth and Planetary Sciences, Weizmann Institute of Science, Rehovot, 76100, Israel

⁴Astronomy Department, University of Washington, Seattle, WA 98195

⁵Institut d'Astrophysique de Paris, 98 bis Boulevard Arago, Paris 75014, France

⁶Guggenheim Fellow

⁷Virtual Planetary Laboratory

⁸Instituto de Astronomía, UNAM, Campus Ensenada, Carretera Tijuana-Ensenada km 103, 22860 Ensenada, B.C. México

⁹Rosseland Centre for Solar Physics, University of Oslo, P.O. Box 1029 Blindern, N-0315 Oslo, Norway

¹⁰Institute of Theoretical Astrophysics, University of Oslo, P.O. Box 1029 Blindern, N-0315 Oslo, Norway

¹¹School of Physics and Astronomy, Monash Centre for Astrophysics (MoCA), Monash University, Clayton, Victoria 3800, Australia

¹²Instituto de Astrofísica de Canarias, C. Vía Láctea S/N, E-38205 La Laguna, Tenerife, Spain

¹³Universidad de La Laguna, Dept. de Astrofísica, E-38206 La Laguna, Tenerife, Spain

¹⁴Aix Marseille Univ, CNRS, LAM, Laboratoire d'Astrophysique de Marseille, Marseille, France

¹⁵Yunnan Observatories, Chinese Academy of Sciences, P.O.Box 110, Kunming 650216, Yunnan Province, China

¹⁶Institut de Cincies de l'Espace (IEEC-CSIC), C/Can Magrans, s/n, Campus UAB, 08193 Bellaterra, Spain

¹⁷Observatori del Montsec (OAdM), Institut d'Estudis Espacials de Catalunya (IEEC), Gran Capit' a, 2-4, Edif. Nexus, 08034 Barcelona, Spain

¹⁸School of Geosciences, Raymond and Beverly Sackler Faculty of Exact Sciences, Tel Aviv University, Tel Aviv, 6997801, Israel

¹⁹Astrophysics Research Centre, Queen's University Belfast, Belfast BT7 1NN, UK

²⁰Leibniz-Institut für Astrophysik Potsdam, An der Sternwarte 16, D-14482 Potsdam, Germany

²¹Hamburg Observatory, Hamburg University, Gojenbergsweg 112, 21029 Hamburg, Germany

²²Institute for Astronomy, Astrophysics, Space Applications and Remote Sensing, National Observatory of Athens, Metaxa & Vas. Pavlou St., Penteli, Athens, Greece

²³Dipartimento di Fisica e Scienze della Terra, Università degli Studi di Ferrara, via Saragat 1, 44122 Ferrara, Italy

²⁴Department of Astronomy & Astrophysics, University of Chicago, Chicago, IL 60637

²⁵Institute of Theoretical Physics and Astronomy, Vilnius University, Sauletekio 3, 10257 Vilnius, Lithuania

²⁶Indian Institute of Astrophysics, Koramangala II block, Bangalore 560034, India

²⁷Instituto de Astronomía, Universidad Católica del Norte, Av. Angamos 0610, Antofagasta, Chile

²⁸Central Astronomical Observatory at Pulkovo of Russian Academy of Sciences, Pulkovskoye shosse d. 65, St. Petersburg, Russia, 196140

²⁹Special Astrophysical Observatory, Russian Academy of Sciences, Nizhny Arkhyz, Russia, 369167

³⁰Kourovka Astronomical Observatory of Ural Federal University,
Mira Str. 19, 620002